Ruscica Romina (Orcid ID: 0000-0003-0127-9579)
Díaz Leandro (Orcid ID: 0000-0002-9237-6704)
Viovoy N (Orcid ID: 0000-0002-9197-6417)

Evapotranspiration trends and variability in southeastern South America: the roles of land-cover change and precipitation variability

Short title: Evapotranspiration trends and variability in southeast. South America

Romina C. Ruscica[a,b,c], Anna A. Sörensson[a,b,c], Leandro B. Diaz[a,b,c], Carolina Vera[a,b,c], Aline Castro[d], Phillip Papastefanou[e], Anja Rammig[e], Luiz F.C. Rezende[d], Boris Sakschewski[f], Kirsten Thonicke[f], Nicolas Viovy[g], Celso von Randow[d]

[a] Universidad de Buenos Aires, Facultad de Ciencias Exactas y Naturales, Departamento de Ciencias de la Atmósfera y los Océanos, Buenos Aires, Argentina

[b] CONICET - Universidad de Buenos Aires. Centro de Investigaciones del Mar y la Atmósfera (CIMA), Buenos Aires, Argentina

[c] CNRS-IRD-CONICET-UBA. Instituto Franco-Argentino para el Estudio del Clima y sus Impactos (UMI 3351 IFAECI), Buenos Aires, Argentina

[d] Impacts, Adaptation and Vulnerability Division, National Institute for Space Research (INPE), São José dos Campos, Brazil

[e] Technical University of Munich, TUM School of Life Sciences, Freising, Germany

[f] Potsdam Institute for Climate Impact Research (PIK), Member of the Leibniz Association, Potsdam, Germany

[g] Le Laboratoire des Sciences du Climat et de l'Environnement (LSCE)

Correspondence: Romina C. Ruscica, Intendente Güiraldes 2160, Ciudad Universitaria, Pabellón II, 2do. piso, C1428EGA, Buenos Aires, Argentina. Email: ruscica@cima.fcen.uba.ar

This article has been accepted for publication and undergone full peer review but has not been through the copyediting, typesetting, pagination and proofreading process which may lead to differences between this version and the Version of Record. Please cite this article as doi: 10.1002/joc.7350

KEYWORDS: South America, Evapotranspiration, Summer variability and trends, Land-cover change, Precipitation variability, Subtropical dipole, Dynamic Global Vegetation Models.

Funding information: CLIMAX Project funded by Belmont Forum/ANR-15-JCL/-0002-01, BMBF FKZ 01LP1610A, and FAPESP-BELMONT- Process 2015/50687-8; Agencia Nacional de Promoción Científica y Tecnológica (ANPCyT), Argentina [PICTs 2017-1406, 2018-02511]; University of Buenos Aires, Argentina [UBACyT20020170100428BA]; SÃO PAULO STATE RESEARCH FOUNDATION [grants 2015/50687-8 and 2017/03048-5] and National Council for Scientific and Technological Development [301084/2020-3]. ORCHIDEE simulations were performed using HPC resources from GENCI-TGCC [2018-6328].

Abstract

Southeastern South America is subject to considerable precipitation variability on seasonal to decadal timescales and has undergone very heavy land-cover changes since the middle of the past century. The influence of local land-cover change and precipitation as drivers of regional evapotranspiration long-term trends and variability remains largely unknown in the region. Here, ensembles of stand-alone Dynamic Global Vegetation Models with different atmospheric forcings are used to disentangle the influence of those two drivers on austral summer evapotranspiration from 1950 to 2010. This paper examines the influence of both the ENSO and the dipole-like first-mode of southeastern South American precipitation variability (EOF1) on regional evapotranspiration. We found that in the lower La Plata Basin, evapotranspiration was driven by precipitation variability and showed a positive summer trend. Moreover, the region showed marked seasonal anomalies during El Niño and La Niña summers but mainly during EOF1 phases. On the contrary, in the upper La Plata Basin, land-cover changes forced the negative summer evapotranspiration trend and particularly reduced the summer anomalies of the late 1990s, a period of ENSO and EOF1-positive phases. In the South Atlantic Convergence

Zone region, the high evapotranspiration uncertainty across ensemble members impeded finding robust results, which highlights the importance of using multiple DGVMs and atmospheric forcings instead of relying on single model/forcing results.

1. Introduction

Evapotranspiration (ET) plays a vital role in shaping climate variability, trends, and extremes and connects the land with the atmosphere (Jung et al. 2010; Wang and Dickinson, 2012; Douville et al. 2013; Teuling et al. 2009; Miralles et al. 2018). ET is driven principally by precipitation and solar radiation variability at different spatial and time scales (Martens et al. 2018) and is constrained by land surface conditions, such as soil moisture and vegetation. Land-cover change (LCC) practices affect the surface energy/water balances modulating ET directly through biophysical (e.g., albedo) and biogeochemical changes (e.g., CO_2 emissions by agricultural activities); and indirectly by runoff or soil erosion, among others (Pielke et al. 2011, Lapola et al. 2014; Mahmood et al. 2014; Perugini et al. 2017). Therefore, evapotranspiration is an integral part of meteorological, hydrological, and biological processes. Here, modelled ET over several decades and its response to precipitation variability and LCC are explored in three South American regions (Fig. 1): South Atlantic Convergence Zone (SACZ), upper La Plata Basin (uLPB), and lower La Plata Basin (lLPB). These highly socio-economically developed regions show notable precipitation trends and variability, and since the middle of the twentieth century, they have undergone intense land-cover changes.

Precipitation in southeastern South America exhibits considerable variability from seasonal to decadal timescales (Vera et al. 2006; Garreaud et al. 2009; Marengo et al. 2012; Grimm et al. 2020). Sea surface temperature conditions of the tropical oceans (e.g. El Niño-Southern Oscillation [ENSO]) and over the polar regions have been identified as remote sources of regional variability that induce precipitation anomalies through distinctive teleconnection patterns in circulation anomalies (e.g., Vera et al. 2006). During

the warm part of the year, the leading continental pattern of interannual precipitation variability is characterized by a dipolar spatial structure with anomaly cores of opposite-sign located over the SACZ and the subtropical plains (lLPB) with the strongest components over the SACZ (e.g., Grimm, 2011, mode 1 in their Fig. 6; Grimm and Zilli, 2009, mode 1 in their Fig. 3). This continental dipole-like mode is weakly connected with ENSO. Here, we focus on a subtropical dipole represented by the first-mode of summer precipitation variability in southeastern South America (SESA region represented in Fig. 1a), hereafter EOF1, whose strongest components occur over lLPB and the opposite weak ones, over SACZ, and is connected with ENSO (Grimm and Zilli, 2009, mode 3 in their Fig. 3). The standard convention associates the positive EOF1 phase (hereafter +EOF1) with wetter-than-normal conditions in lLPB and drier-than-normal conditions in SACZ. In contrast, the negative phase (hereafter -EOF1) represents the opposite situation (e.g., Doyle and Barros, 2002; Diaz and Vera, 2017). Wetter-than-normal (drier-than-normal) conditions are more common in lLPB during El Niño (La Niña) austral summer (DJF), while the response over the SACZ region is less clear and is more sensitive to the specific area or month analyzed (e.g., Grimm, 2003, 2004; Cai et al. 2020). In lLPB, precipitation has shown a positive trend since the beginning of the 20th century (Gonzalez et al. 2013; Zhang et al. 2016a; Saurral et al. 2017). The austral summer trend can be at least partially explained by the increase of greenhouse gas concentrations by human activities (e.g., Vera and Diaz, 2015). Moreover, using both observations and climate model outputs, Diaz and Vera (2017) showed that the positive DJF trend in lLPB is in part associated with an increase (decrease) of the frequency of +EOF1 (-EOF1) events from the early 20th century to the present. Negative but not significant DJF trends in precipitation anomalies over SACZ have been detected for the same period (Vera and Diaz, 2015). In addition, the anthropogenic climate change signal in both regions could be affected by natural interdecadal variability (e.g. Grimm and Saboia, 2015; Dai, 2021).

Although a less explored connection, ET and land surface conditions also play an essential role in precipitation variability (Sörensson and Menéndez, 2010; Ruscica et al. 2015; Giles

et al. 2020). They shape climate, even influencing the relationship between the main continental variability modes of spring and summer (Grimm et al. 2007; Grimm and Zilli, 2009). For instance, the dipole-like first variability mode has been found recently in the main variability patterns of two vegetation indices during the austral spring season (Chug and Dominguez, 2019).

Southeastern South America has suffered different types of LCC (Salazar et al. 2015). SACZ and uLPB include parts of the seasonally-dry Cerrado and Atlantic Forest ecosystems, where native vegetation has been reduced drastically to expand cattle ranching and to cultivate sugarcane and soybean (Lapola et al. 2014). The continental-scale land cover evidenced an extreme change in uLPB and eastern SACZ between 1950 and 2010, leaving only around 25% of natural vegetation by 2010 (Fig. 1b,c). The lLPB includes most of the subhumid temperate Pampas Plains where native grasslands have been converted to croplands (e.g., soybean, wheat) at increasing rates, and recently even to exotic tree plantations (Nosetto et al. 2012). While the type of LCC in each region is well known, less is known about how this change forces near-surface variables. Different ET responses have been found depending on the methodological approach (Lee and Berbery, 2012); on the crop seasonal cycle stage (e.g., Georgescu et al. 2013); and/or on the type of native vegetation (Beltrán-Przekurat et al. 2012).

Understanding how LCC affects regional ET dynamics requires the use of models, given the complexity of the processes involved and the scarcity of measurements (Lawrence and Vandecar, 2015; IPCC SRCCL, Jia et al. 2019). Dynamic Global Vegetation Models (DGVMs) simulate surface processes ranging from the transfer of energy, water, and momentum between the land surface and the atmosphere; through biogeochemical cycles, carbon assimilation and allocation, plant phenology, to land-use change (Prentice et al. 2007; Rezende et al. 2015). Stand-alone DGVMs (forced by atmospheric data) allow obtaining land-surface variables at large spatial and long temporal scales to answer questions related to water resources. However, the modelling of ET involves many

uncertainties (Mueller et al. 2011; Jiménez et al. 2011), such as the choice of atmospheric forcing data (Badgley et al. 2015) or the LCC scenario (Douville et al. 2013). Moreover, DGVMs still miss the representation of other processes such as plant hydraulics strategies, which are essential to a correct simulation of how quickly plants react to droughts (Papastefanou et al. 2020). In particular, land-surface models and DGVMs show large ET uncertainties in South America (Sörensson and Ruscica, 2018; Sakschewski et al. 2021). So far, only some global studies have analyzed long-term ET evolution using stand-alone DGVMs (e.g. Douville et al. 2013; Livneh et al. 2013). To evaluate the role of LCC in ET, related uncertainties and regional gaps, we performed an ensemble of simulations over South America with four state-of-the-art DGVMs (INLAND, LPJmL4, LPJ-GUESS, and ORCHIDEE (v2.0)), which have been applied in other studies (e.g., ISIMIP (https://www.isimip.org/), Guimberteau et al. 2017).

This study aims to find out how precipitation variability and/or LCC affected ET in SACZ, uLPB, and lLPB, during 1950–2010. To that end, we explored regional ET seasonality, DJF trends, and anomalies in simulations with and without LCC information and using composites of ENSO and EOF1 summers. ET monthly data in 0.5°x0.5° grid resolution were taken from a new ensemble of 24 stand-alone DGVM simulations, a product of the CLIMAX project (http://www.climax-sa.org). The DGVMs were run offline, so feedbacks from the land to the atmosphere were not considered. All the data and the ENSO/EOF1 definition are described in section 2, and a climate characterization of each region is made in Section 3. Section 4 shows evapotranspiration results and discussion, and conclusions are presented in section 5.

2. Data and methodology

2.1. Simulations and gridded products

We performed 24 simulations over South America based on the combination of four DGVMs forced by three atmospheric datasets, each using two different land-cover

conditions (Fig. 2, top): observed land-cover changes (LCC) and potential natural vegetation (PNV). The PNV concept refers to the expected state of mature vegetation conditions in the absence of human activities (e.g., Chiarucci et al. 2010). Here each DGVM uses its own set of criteria to define PNV. On the other hand, LCC annual data combine two historical land-use datasets that are shared by all LCC simulations. Fig. 1(b, c) shows these LCC data as fractions of natural vegetation in the first and last years of the analyzed period in South America. Table 1 summarizes the information and references about LCC data, DGVMs, and atmospheric forcing datasets (GLDAS_2.0, GSWP3, and WATCH+WFDEI) as well as about three ET gridded global products (GLDAS_2.0, GLEAM_3.3a, and PML) used as reference data for DGVM comparison. It is important to note that although GLDAS_2.0 is one of the atmospheric forcings, it also includes ET as a variable. All datasets have a monthly time step and a spatial resolution of 0.5° x 0.5°, except GLEAM_3.3a, which is available at 0.25°x0.25°. The analyses were done over the 1950–2010 time period, except for the analysis of austral summers (1951–2010) and the model comparison to reference data (1980–2010). Following the same simulation protocol, DGVMs were executed with vegetation spin-ups ranging from 1000 to 2000 years to achieve equilibrium between climate and vegetation.

LPJmL4, LPJ-GUESS, and INLAND models were originally developed as DGVMs; ORCHIDEE, on the other hand, was originally developed as a Land Surface Model. These DGVMs have distinct configuration structures (time step, soil depth, vegetation characteristics) and therefore they need different sets of forcing variables (Table 1).

2.2. Definition of multi-model ensembles

Sub-samples of the 24 simulations were clustered in five Multi-Model Ensembles (hereafter MME): MME_{GLDAS}, MME_{MOD}, and MME_{FORC} for the LCC case only; and for both cases MME_{LCC} and MME_{PNV} (Fig. 2, bottom). Note that simulations (s) are tagged with a number (e.g. s5) at the top of Fig. 2 to indicate the composition of the multi-model ensembles.

DGVMs ability to describe the seasonal evolution of ET monthly means and the corresponding interannual variability during 1950–2010 is assessed in section 4.1. The mean and individual members of the 4-member MME_{GLDAS} are compared with the GLDAS_2.0 data as a reference. This analysis will allow a direct comparison among DGVMs since we focus on one atmospheric forcing dataset only (GLDAS_2.0) which is also consistent with the ET GLDAS_2.0 reference data (the only dataset available for the period 1950–2010). Moreover, ET from GLDAS_2.0 has been used in other studies of South America (e.g., Spennemann and Saulo, 2015).

MME_{MOD} and MME_{FORC} are defined to distinguish the ET uncertainty from DGVMs from the ET uncertainty in the forcing data, respectively. Moreover, since uncertainty levels present in ET gridded reference datasets over South America are not negligible (Sörensson and Ruscica, 2018), both MME_{MOD} and MME_{FORC} are compared to the ensemble of ET reference datasets (GLDAS_2.0, GLEAM_3.3a, and PML, see Table 1) in section 4.2. In this case, the period is reduced to 1980–2010 since GLEAM_3.3a and PML are based on satellite information, which was made available widely in the 1980s.

Finally, MME_{LCC} and MME_{PNV} are employed to describe the characteristics of the trend, variability, and extremes of ET anomalies in the three regions of study for the period 1951–2010 (section 4.3). With this choice, we want to analyze the influence of LCC on ET long-term dynamics, differently from the analyses in Sections 4.1 and 4.2, where we focus on DGVM and forcing uncertainties related to the seasonal cycle only. Particular focus is made on the summer season —DJF— when precipitation trends and variability are remarkable. MME_{LCC} and MME_{PNV} results are shown with boxplots, highlighting their medians, which were analyzed statistically with the Wilcoxon rank test (Gibbons and Chakraborti, 2011; Hollander and Wolfe, 1999). It is a paired difference test that can be used as an alternative to the paired Student's t-test when the distribution of the difference between two sample means cannot be assumed to be normally distributed. The MME spread is defined as the interquartile range of each boxplot. As the same

atmospheric forcings drive both types of experiments (LCC and PNV), the differences between results will identify the impact of land-cover changes on regional evapotranspiration.

2.3. Selection of summer ENSO and EOF1 events

Historical ENSO episodes are identified using the Oceanic Niño Index (ONI) developed by NOAA's Climate Prediction Center (CPC, online at https://origin.cpc.ncep.noaa.gov/products/analysis_monitoring/ensostuff/ONI_v5.php). The ONI is computed from 3-month running mean values of ERSST.v5 sea surface temperature (Huang et al. 2017) anomalies in the Niño 3.4 region. El Niño (EN) events are characterized by a positive ONI greater than or equal to +0.5°C, while La Niña (LN) events are characterized by ONI values less than or equal to −0.5°C, for a period of at least 5 consecutive overlapping 3-month seasons according to CPC definition.

The influence of the activity of the year-to-year summer rainfall variability leading pattern (EOF1) is also assessed. Following Díaz and Vera (2017), the EOF1 was obtained as the first mode of an Empirical Orthogonal Function (EOF) analysis applied over the subtropical SESA domain encompassed between 39°–16°S and 64°–31°W (dashed rectangle in Fig. 1a). The EOF applied was computed using the DJF precipitation anomalies of each of the three atmospheric forcing datasets (Table 1). Each EOF1 temporal evolution is described through its corresponding principal component time series. Fig.1a shows the correlation pattern between DJF precipitation anomalies at each SESA point with the temporal evolution of subtropical EOF1, computed with the GLDAS_2.0 database as an example (GSWP3 and WATCH+WFDEI yield similar results). To define positive and negative events of the EOF1, we averaged the EOF1 temporal evolution of the three datasets. Positive (negative) EOF1 events are defined as those DJF for which the average is larger (smaller) than 1 (-1) standard deviation of the 1951–2010 period.

Table 2 summarizes DJFs that are identified as ENSO (EN, LN) and/or EOF1 events. In total, 22 EN, 18 LN, 10 positive EOF1 (+EOF1), and 10 negative EOF1 (-EOF1) events are identified within the 1951–2010 period. Note that some DJFs are identified twice, for example, 2009 is both an LN event and a -EOF1 event.

3. Regions: climate characterization

While the lLPB and SACZ regions are defined considering the dipole-like spatial structure and localization of the main cores of action of the subtropical EOF1 (Fig. 1a), the motivation for studying uLPB relies on the maximum native vegetation reduction in the entire continent (Fig. 1c). As a result, SACZ is comprised between 22°–14°S and 47°–39°W but without the southwestern corner comprised between 19°S and 22°S and 47°W and 44°W; lLPB is between 36°–27°S and 62°–50°W; and uLPB, between 26°–19°S and 57°–47°W.

The climatic features of SACZ, lLPB, and uLPB are explored through the mean seasonal cycle and interannual variability of monthly values of precipitation and incoming shortwave radiation (Fig. 3). The ensemble mean and spread (i.e., max–min) of the three atmospheric forcing datasets (Table 1) are used for such purposes. Mean seasonal cycles (Fig. 3A) show that SACZ and lLPB have a kind of opposite behaviour regarding the annual amplitude of both variables. SACZ has a marked monsoon regime with heavy summer rainfall and a marked dry JJA season (Fig. 3a) with low amplitude in the annual radiation cycle (Fig. 3b). lLPB does not have a marked dry season (Fig. 3e) and incoming radiation follows the solar cycle with marked amplitude (Fig. 3f). uLPB shows a wet summer and a lighter dry season in late winter in respect to SACZ (Fig. 3c); its radiation cycle minimizes in June, but maximizes earlier in November (lLPB/SACZ peaks in December/February) (Fig. 3d). Note that the greatest spread in the representation of the annual cycle of radiation corresponds to SACZ (Fig. 3b).

Interannual variability (Fig. 3B) of precipitation shows similar behaviour to the mean annual cycle (larger rainfall volumes imply more rainfall variability (e.g., Garreaud et al. 2009)), with lower values. Regarding incoming radiation, the largest amplitude is now seen in SACZ (Fig. 3h) and reduced in lLPB (Fig. 3l), which is quite similar to uLPB (Fig. 3j). Note that the spread among atmospheric datasets is larger for radiation than for precipitation.

4. Evapotranspiration results and discussion

4.1. Seasonal cycle

To evaluate the annual cycle of ET in the entire simulation period, we analyzed ET seasonality from DGVMs forced only by the GLDAS_2.0 atmospheric dataset (members in MME_{GLDAS}) and compared it to the ET GLDAS_2.0 reference data for the 1950–2010 period (Fig. 4). GLDAS_2.0 is the only forcing dataset that includes ET information and the only reference dataset that goes back to 1950.

ET mean annual cycles evidence seasonality with values ranging from 20 to 120 mm/month approximately (Fig. 4a, b, c). Unlike the seasonal cycles of precipitation and radiation, ET annual cycles are quite similar among regions. The MME_{GLDAS} mean (black line) is closer to the reference dataset (magenta line) than individual simulations, with values lower than GLDAS_2.0 ones in all regions (mainly in lLPB) and months, except during the beginning of the wet season in SACZ (SON) and uLPB (SO) when they are equal. Note that the MME_{GLDAS} mean in SACZ/lLPB tends to follow the annual cycle of precipitation (Fig. 3a) / incoming radiation (Fig. 3f). This behaviour somehow explains why the timing of the ET minimum is different in each region, being it August in SACZ and June in lLPB. On the intra-annual scale, ET responds more directly to precipitation in SACZ. In lLPB, it responds more to radiation because of water availability throughout the year; however, energy for latent heat is limited in winter. ET reacts differently in uLPB, with a

maximum in January (as in precipitation, Fig. 3c) and a minimum in June (as in radiation, Fig. 3d). The spread among MME_{GLDAS} components exhibits seasonal variations too. The best agreement among DGVMs occurs in lLPB during winter months when atmospheric demand (i.e., radiation) is relatively low, and in SACZ with the ending of the dry season when this demand (partially) maximizes. uLPB stands out as the region where the disagreement among DGVMs occurs all year long, probably because precipitation and radiation never reach such low minimum values as seen in SACZ and lLPB. Across the three regions, LPJmL4 and LPJ-GUESS behave similarly and reproduce the GLDAS_2.0 relative minimum in February, while ORCHIDEE is a lower outlier. INLAND is an upper outlier just in SACZ and uLPB since in lLPB, it is overpassed by GLDAS_2.0 which lies mainly beyond the DGVM spread.

The seasonal evolution of the interannual variability of ET monthly values differs among regions (Fig. 4d, e, f). In contrast to the seasonal cycles of precipitation and radiation, annual cycles in SACZ and uLPB are distinct with prominent peaks in October and September, respectively. In SACZ, such peak occurs after a very dry winter (Fig. 3a) with too low soil water storage followed by an increment in incoming radiation entering spring (Fig. 3b). With these surface conditions, the remotely driven early or late beginning of the monsoon season makes much difference to ET (Grimm et al. 2007). The DGVMs highly agree on the ET peak and highly disagree during the rest of the year when the DGVM spread is vast. For example, no decrease is observed in the interannual variability of INLAND ET during the dry season in SACZ (Fig. 4d), probably because absolute ET is high during these months (Fig. 4a). Variability in lLPB (Fig. 4f) is similar to that of the mean seasonal cycle (Fig. 4c) as it was seen in precipitation (Fig. 3b,k), with more agreement among DGVMs during cold months. MME_{GLDAS} mean values are still generally lower than GLDAS_2.0 ones, though only in lLPB (Fig. 4f). The opposite occurs in SACZ and uLPB (Fig. 4d, e).

4.2. Sources of uncertainty

The role of DGVMs versus that of atmospheric forcing (used by the DGVM) in contributing to the uncertainties associated with the mean seasonal cycle of ET is further analyzed. The uncertainty due to DGVMs is quantified by the spread between members of MME_{MOD} and the uncertainty due to forcings, by the spread between members of MME_{FORC} (section 2.2 for MME compositions). Fig. 5 shows a much larger spread in MME_{MOD} (light grey band) than in MME_{FORC} (dark grey band) where the spread is almost zero in many months. This means that the differences in DGVMs provide larger uncertainty ranges in ET seasonality than those emerging from differences in atmospheric forcings. At this mean monthly scale, the low ET uncertainty due to forcings is consistent with the low uncertainty in both precipitation and radiation forcings (Fig. 3A).

Moreover, and unlike the previous section where only GLDAS_2.0 was considered as ET reference dataset, here we present the uncertainty existing in the ensemble of three ET reference datasets and in a shorter period (section 2.1). Uncertainty (light magenta band) is present almost all year in SACZ (Fig. 5a) and lLPB (Fig. 5c), and notably from April to August in uLPB (Fig. 5c).

If we now focus on ensemble means, the annual cycles are represented with black lines for modelled ET and magenta lines for ET reference data. Note that the black line represents the MME_{LCC} mean which is equal to the MME_{MOD} mean and to the MME_{FORC} mean because of how the ensembles were built (Fig. 2). Consequently, these lines show the most general ET comparison between the whole multi-model ensemble and the reference data for a shorter period of 31 years (the annual cycle of MME_{LCC} of the long 61-year period was very similar, not shown). Analogously to Fig. 4, MME_{LCC} mean values are generally lower than the means of the reference dataset even though this difference is smaller in Fig. 5. In other words, the comparison between Fig. 5 and Fig. 4 made it possible to identify GLDAS_2.0 as an upper outlier in respect to both satellite-based ET reference products, mainly for the winter months in lLPB (magenta line in Fig. 4c is shifted to lower values in Fig. 5c). The original reasons for using ET from GLDAS_2.0 were its long-period

(equal to the multi-model ensemble) and its consistency as one of the atmospheric forcings used for the simulations. However, although ET data in GLDAS_2.0 are obtained similarly to ET in DGVMs, the land surface model used to obtain GLDAS_2.0 data (Noah) disregards the temporal variability of vegetation unlike other ET sources (DGVMs, GLEAM_3.3a, and PML).

4.3. Summer evapotranspiration dynamics

4.3.1. Evapotranspiration trends

Austral summer ET linear trend magnitudes were estimated for each region through linear least square regression analysis using Pearson's correlation and are displayed in Fig. 6. In this figure, trends are shown for each MME_{LCC} and MME_{PNV} simulation (as described in Fig. 2) and also with boxplots for each MME in both scenarios (each boxplot includes a sample of 12 trends). Trends in the GLDAS_2.0 reference dataset (magenta dots) are shown for comparison, but they are not statistically significant.

In SACZ and uLPB, there is marked uncertainty in the sign of trends, with values going from -10 to +12 mm/season/decade. This uncertainty is mainly associated with DGVM response to different atmospheric forcings. For example, the largest robust ET trends for all DGVMs, regions, and scenarios were obtained from simulations driven by the WATCH+WFDEI atmospheric forcing (squares). WATCH+WFDEI radiation behaves differently from the other two forcings (not shown) and could be the reason for the different trends. On the contrary, and with a less pronounced response, GLDAS_2.0 forcing (circles) causes significant negative ET trends in the LCC scenario. These results highlight the importance of trends in forcing precipitation and other ET drivers such as radiation (Teuling et al. 2009) or vapour pressure deficit (Barkhordarian et. al. 2019). On the other hand, lLPB shows the lowest uncertainty, with robustly positive trends and values roughly between 2 and 4 mm/season/decade. LPJmL4 differs from the rest of the DGVMs and shows the largest trend with the lowest forcing uncertainty.

The analysis of MME medians reveals that no trend signal is seen over SACZ (median not different from 0); lLPB shows significant positive trends (p=0.5); and uLPB has a significant trend of -3.15mm/season/decade in the LCC scenario significantly differing from the missing trend in the PNV case. Note that although uLPB shows a large MME spread (as SACZ), the median MME trend responds to the LCC effect significantly.

Therefore, land-cover change is not a dominant factor in explaining the positive evapotranspiration trend over lLPB but it is probably the cause for the negative ET trend in uLPB. The LCC effect on surface fluxes seems easier to estimate in regions such as uLPB where land conversion was made from forests. This can be partially explained by the fact that in lLPB, changes have been mainly from grasslands to croplands instead of from forest to cropland (Salazar et al. 2015). Since grasslands and cropland have similar rates of ET, smaller differences can be expected than in uLPB. Moreover, in the lLPB domain defined for this study, the change in the fraction of natural vegetation between 1950 and 2010 is not meaningful (Fig. 1b, c).

4.3.2. ET response to main modes of precipitation variability

Detrended DJF ET anomalies were computed from the MME_{LCC} and MME_{PNV}. To assess the influence of ENSO on ET variability, we calculated the ET seasonal anomaly averaged over the 22 EN and 18 LN ENSO-events (Table 2) for each of the 12 MME members. Fig. 7 shows the boxplots of the 12 MME ET anomalies as well as GLDAS_2.0 ET anomalies. MME anomalies are relatively small in magnitude for EN events over SACZ and uLPB with negative and positive values, respectively. Most anomalies in LN events are negligible (MME medians not different from 0). On the other hand, ET anomalies over lLPB are all positive in EN events with magnitudes around +10 mm/season. In LN events, all anomalies are negative with magnitudes around -10mm/season. Differently, the MME spread presents asymmetric behaviour, with a lower interquartile range in LN than in EN events.

The influence of the leading pattern of southeastern South American precipitation variability, EOF1, was also assessed in the same figure. Mostly in lLPB and to a lesser

degree in uLPB, the behaviour of composites with smaller sub-samples of ET anomalies (ten +EOF1s and ten -EOF1s, Table 2) is similar to that observed for precipitation, i.e., positive anomalies for +EOF1 and negative for -EOF1. The opposite phase but with low median values is seen in SACZ. GLDAS_2.0 DJF ET anomalies are found statistically significant in all cases (EN, LN, EOF1s) for lLPB, and in the +EOF1 case for uLPB. These anomalies are consistent in sign with MME median values, with better matching in EOF1s than in ENSO cases.

Overall, the MME median and spread during EOF1 DJF events are higher than during ENSO. Therefore, DJF ET anomalies seem to be more affected by regional precipitation variability than by large-scale variability. However, DJF ENSO and EOF1 events are not independent, and the number of ENSO events doubles that of EOF1 events (Table 2). Note that in SACZ, the low ET response to ENSO and EOF1 phases is coherent with the fact that the summer continental first mode, with strongest dipole component over the SACZ and weaker component of opposite sign over lLPB, does not have significant connection with ENSO (first mode in Grimm 2011; Grimm and Zilli, 2009). Yet, the EOF1 used as reference in this manuscript is a subtropical mode (domain over SESA, Fig. 1a) with the strongest dipole component over lLPB and weaker ones of opposite sign over SACZ. Therefore, higher median values of the anomalies in lLPB (Fig. 7) are expected, since this mode represents the variability in lLPB much better than in SACZ and it is connected with ENSO because lLPB is much affected by ENSO. This mode is similar to summer mode 3 in Grimm and Zilli (2009), which is connected to ENSO and also presents a trend.

These results were mostly valid for MME_{LCC} and MME_{PNV} since no significant difference between median anomalies of MME_{LCC} and MME_{PNV} was found in this analysis.

4.3.3. ET interannual variability and extremes

The subsequent analysis focuses on lLPB and uLPB regions since SACZ results were not robust. In Fig. 8, the temporal evolution of linear detrended summer ET anomalies is

represented for each DJF by boxplots of the corresponding MME_{LCC} and MME_{PNV} values. DJF anomalies of GLDAS_2.0 reference data are added for comparison.

Since ET summer anomalies over lLPB resemble clearly the corresponding precipitation anomalies during ENSO and EOF1 events, as described in the past section, high negative (positive) ET absolute anomalies will indicate dry (wet) summers. In Fig. 8a, robust results were obtained for more than one third of DJFs, i.e., all members of the MME_{LCC} show the same anomaly sign. Of those "robust" wet (dry) DJFs, two thirds and one third are identified as EN and +EOF1 (LN and -EOF1), respectively (Table 2). In particular, the commonly agreed precipitation sign behaviour is seen in ET, mainly in the wet 1998 and 2010 EN/+EOF1 events and the dry 1965 and 2009 LN/-EOF1 events. On the other hand, the -EOF1/EN 1952 event is identified as dry, while the +EOF1/LN 2001 is wet. These results would indicate that EN (LN) is not the only driver of climate anomalies leading to wet (dry) conditions in lLPB.

According to the literature, the dry LN/-EOF1 DJF of 1965 recorded a moderate drought. The driest summer occurred in 1989 during LN (median of -54.1 mm/season) and was identified within a prolonged drought that significantly decreased corn productivity in the region (Rivera and Penalba, 2014). The second driest summer was LN/-EOF1 2009 with -50.1mm/season, reflecting the 2008/9 macro-regional extreme drought over southern South America (Müller et al. 2014; Spinoni et al. 2019). The wettest DJFs took place during the last decade of the whole period with +42.7mm/season in the EN/+EOF1 2010 followed by +37.8mm/season in 2003. Note that dry summers are more extreme than wet summers in terms of magnitude of ET anomalies, as there is possibly an atmospheric upper limit to ET, while no lower limit exists. The same happens with GLDAS_2.0 extremes, which show particularly large negative anomalies in the mentioned dry summers of 1965, 1989, and 2009.

Larger DJF ET anomalies and interannual variability are seen in lLPB as compared to uLPB (Fig. 8b) (as also shown in Fig. 4 and Fig. 7). The standard deviation as a measure of the

interannual variability of the MME_{LCC} median time series is 22mm/season in lLPB and 8mm/season in uLPB. GLDAS_2.0 also detects the larger variability in lLPB (31mm/season) as compared to uLPB (12mm/season). The large ET interannual variability in lLPB is consistent with large DJF surface variability (Ruscica et al. 2016; Spennemann et al. 2018), particularly in temperature (Menéndez et al. 2016; 2019). In line with the previous analysis, ET changes due to LCC are less significant in lLPB than in uLPB. The interannual variability of PNV almost equals the interannual variability of LCC (21mm/season) and there is practically no significant difference between medians ($p>=0.37$). The wet El Niño 2007 is the only exception, with the median of MME_{LCC} exceeding the positive median of MME_{PNV} by 50% ($p=0.08$); however, these anomalies are below 15mm/season.

In uLPB, ET is sensitive to LCC, which is seen in the 15% reduction in interannual variability from PNV to LCC; and in the median anomalies during three consecutive summers in the late 1990s. Fig. 8b shows that positive anomalies disappear in 1997 ($p=0.04$) and drop by 45% in 1999 ($p=0.02$) because of LCC. To a lesser degree, LCC also reduced the positive ET anomaly by 35% in 1998 ($p=0.2$). According to Table 2, summers were neutral (but almost +EOF1) in 1997, EN/+EOF1 in 1998, and LN in 1999. Some global studies have found a high ET mean during the 1997–98 period identified as an intense EN (Jung et al. 2010; Douville et al. 2013). It turns out that these three summers that showed a robust reduction in positive ET anomalies due to LCC, were under well-defined ENSO and positive dipole phase conditions. These results are validated by the GLDAS_2.0 reference dataset that shows anomalies falling within MME ranges, particularly during the late 1990s.

The smaller spreads in MME_{LCC} compared to MME_{PNV} can be explained by the fact that all MME_{LCC} members were obtained with the same LCC data while in MME_{PNV} there is a larger dependency on the geographical distribution of natural vegetation simulated by each DGVM.

5. Summary and conclusions

The effect of historical land-cover changes (LCC) and precipitation variability on modelled evapotranspiration (ET) seasonality, and DJF summer trends and variability were analyzed over three regions in southeastern South America. ET data were taken from a new ensemble of 24 monthly, 50x50km^2 stand-alone DGVM simulations for 1950–2010, a product of the CLIMAX project (http://www.climax-sa.org/). The ET annual cycle behaviour of DGVMs was found to be similar to the GLDAS_2.0, GLEAM_3.3a, and PML reference datasets. This ET seasonal analysis also showed that DGVMs mostly agree when mean values reach their minimum during cold and dry months and when interannual variability peaks at the beginning of the monsoon season. Fig. 9 summarizes the main findings in each region.

ET uncertainties were more pronounced over SACZ, a region with a marked monsoon regime where ET was found to depend on precipitation seasonality mostly. However, there is little agreement on the main drivers of ET in the SACZ region which has been defined both as energy-limited —where ET is mostly driven by the atmosphere (Spennemann and Saulo, 2015; Menéndez et al. 2016)— and as water-limited (Zhang et al. 2016c; Sörensson and Ruscica, 2018). This contradiction could be due to uncertainties in atmospheric drivers, as we found here for radiation. Differences in how the applied DGVMs represent the response of vegetation and ET to atmospheric drivers cause considerable uncertainty in the annual cycles of both the mean values and the standard deviations of simulated ET. Previous studies have also found notable differences among ET monthly anomalies from different ET datasets (Sörensson and Ruscica, 2018) and among absolute ET values (Pereira et al. 2017) in central-eastern Brazil. During DJF months, the interannual variability of radiation and precipitation in SACZ is larger than in uLPB and lLPB. The response of ET to precipitation modes of variability and the ET trend signal were not robust, in line with the non-significant precipitation trend found in Vera and Diaz (2015). In summary, the uncertainty in modelled ET impedes finding a clear ET response to

land and atmospheric conditions in SACZ, which highlights the importance of using multiple DGVMs and atmospheric forcings instead of relying on the results of a single model or forcing factor.

In the radiation-limited lLPB region, no clear response was seen of ET to LCC, probably because the historical LCC between 1950 and 2010 was not so marked in that region, but also because the vegetation types there (grasslands and/or croplands) have similar ET rates. On the other hand, ET showed robust responses to regional and large-scale variability of precipitation in lLPB. A positive DJF ET trend was simulated coherently with the known positive observed precipitation trend over the region (Diaz and Vera, 2017). Consistently with the known sign in precipitation anomalies, ET DJF anomalies were positive (negative) in EN and +EOF1 (LN and -EOF1) event composites. This is consistent with Miralles et al. (2014) who found a significant correlation between GLEAM monthly anomalies of ET and an ENSO index in some parts of lLPB (see their Fig. 3a), in the last 30 years of our study period. Another close influence of precipitation on ET was indirectly detected in some extreme summer anomalies related to droughts in lLPB (Müller et al. 2014; Spinoni et al. 2019). Moreover, the largest summer interannual variability of ET was consistent with the fact that lLPB has been identified as a hotspot of land-atmosphere interaction (Spennemann et al. 2018). In this region, all the modelled ET statistics (trend, anomalies, variability) were mostly consistent with the behaviour of the GLDAS_2.0 ET reference dataset.

Although both lLPB and SACZ regions were defined over the main anomaly cores of the subtropical precipitation dipole (EOF1), ET trends and variability were robust in the former region and uncertain in the latter. This could be related to the asymmetry of the analyzed dipole, which has a stronger component over lLPB than over SACZ (our Fig. 1a). This asymmetry was seen in the continental EOF3 shown in Grimm and Zilli (2009), who also found a significant trend (till late 1990s) and a stronger relationship to ENSO. On the other hand, ET anomalies and associated spread were larger during active dipole phases than

during ENSO phases, since EOF1s capture regional precipitation variability better than ENSO indices (e.g., Grimm et al. 2007).

The region with the most intense LCC is uLPB, with only 20% of natural vegetation left in 2010 in respect to 1950. Coherently, we found a significant negative DJF ET trend during this period, which could not be confirmed with the only ET reference dataset available for the period 1951–2010 (GLDAS_2.0, Noah–land surface model). Changes in vegetation are usually not implemented in these kinds of land surface models, which lead to a false representation of trends in ET components, such as transpiration (Zhang et al. 2016). LCC significantly reduced positive DJF ET anomalies in the late 1990s, which according to Tucci and Clarke (1998), was when forested areas were reduced to less than 20% of their size in the 1950s. Moreover, it was a period that included a positive dipole phase and the warm ENSO of 1997–98. However, the magnitude of DJF ET anomalies during ENSO/EOF1s composites was low. Therefore, ET dynamics in uLPB was found to be driven by LCC but not by precipitation variability, a behaviour also observed in river discharge (Tucci and Clarke, 1998; Saurral et al. 2008; Doyle and Barros, 2010).

The DGVMs used in this study differ in terms of processes and vegetation-type parameterization (i.e., plant functional types), so they require different sets of forcings. While LPJmL4 and LPJ-GUESS use precipitation, temperature, and downward shortwave radiation as input; INLAND and ORCHIDEE additionally need downward longwave radiation as well as wind speed and specific humidity at 2m. LPJ-GUESS and LPJmL4 represent some processes similarly, such as photosynthesis and evapotranspiration, but differ in representing vegetation dynamics. These differences amongst DGVMs were important for the modelled seasonal cycle of ET, which resulted to be more related to the DGVM structure than to the atmospheric forcing dataset. On the contrary, ET trends were found to be more dependent on the forcing datasets than on the DGVMs. Specifically, radiative forcing introduces a source of high uncertainty on modelled ET (e.g., Badgley et al. 2015). Note that there is no contradiction regarding the cause of modelled ET

uncertainties (DGVM and forcings), since we examined different statistics such as seasonality and trends, as shown in Sörensson and Ruscica (2018). Similar DGVM divergences due to internal processes and climatic forcings are also found in Rezende et al. (2021, unpublished data) who explore anthropogenic effects on vegetation productivity and evapotranspiration in the southern Amazon.

Finally, we want to emphasize that since we used uncoupled simulations, we were unable to analyze the effects of the land surface, i.e., evapotranspiration, on the atmosphere. In a coupled system, reduced ET could lead to reduced or enhanced rainfall by inducing non-local circulation changes in lower-level moisture fluxes and in the convergence of those fluxes (Grimm et al. 2007; Lee and Berbery, 2012; Pereira et al. 2017; Giles et al. 2020). These complex processes should be subject of future studies to improve the knowledge of land-atmosphere interactions in a system under intense and dynamic anthropogenic actions, such as land-cover changes.

7. Bibliography

Badgley, G., Fisher, J.B., Jiménez, C., Tu, K.P., Vinukollu, R. (2015) On Uncertainty in Global Terrestrial Evapotranspiration Estimates from Choice of Input Forcing Datasets. *Journal of Hydrometeorology* 16, 1449–1455. doi:10.1175/jhm-d-14-0040.1.

Barkhordarian, A., Saatchi, S.S., Behrangi, A., Loikith, P.C., Mechoso, C.R. (2019) A Recent Systematic Increase in Vapor Pressure Deficit over Tropical South America. *Scientific Reports* 9, 15331. doi:10.1038/s41598-019-51857-8.

Beltrán-Przekurat, A., Sr, R.A.P., Eastman, J.L., Coughenour, M.B. (2012) Modelling the effects of land-use/land-cover changes on the near-surface atmosphere in southern South America. *International Journal of Climatology* 32, 1206–1225. doi:10.1002/joc.2346.

Cai, W., McPhaden, M.J., Grimm, A.M., Rodrigues, R.R., Taschetto, A.S., Garreaud, R.D., Dewitte, B., Poveda, G., Ham, Y.-G., Santoso, A., Ng, B., Anderson, W., Wang, G.,

Geng, T., Jo, H.-S., Marengo, J.A., Alves, L.M., Osman, M., Li, S., Wu, L., Karamperidou, C., Takahashi, K., Vera, C. (2020) Climate impacts of the El Niño–Southern Oscillation on South America. *Nature Reviews Earth & Environment* 1, 215–231 (2020). doi:10.1038/s43017-020-0040-3.

Chiarucci, A., Araújo, M.B., Decocq, G., Beierkuhnlein, C., Fernández-Palacios, J.M. (2010) The concept of potential natural vegetation: an epitaph? *Journal of Vegetation Science* 21, 1172–1178. doi:10.1111/j.1654-1103.2010.01218.x.

Chug, D., Dominguez, F. (2019) Isolating the Observed Influence of Vegetation Variability on the Climate of La Plata River Basin. *Journal of Climate* 32, 4473–4490. doi:10.1175/jcli-d-18-0677.1.

Dai, A. (2021) Hydroclimatic trends during 1950–2018 over global land. *Climate Dynamics* 56, 4027–4049. doi:10.1007/s00382-021-05684-1.

Díaz, L.B., Vera, C.S. (2017) Austral summer precipitation interannual variability and trends over Southeastern South America in CMIP5 models. *International Journal of Climatology* 37, 681–695. doi:10.1002/joc.5031.

Douville, H., Ribes, A., Decharme, B., Alkama, R., Sheffield, J. (2013) Anthropogenic influence on multidecadal changes in reconstructed global evapotranspiration. *Nature Climate Change* 3, 59–62. doi:10.1038/nclimate1632.

Doyle, M.E., Barros, V.R. (2002) Midsummer Low-Level Circulation and Precipitation in Subtropical South America and Related Sea Surface Temperature Anomalies in the South Atlantic. *Journal of Climate* 15, 3394–3410. doi:10.1175/1520-0442(2002)015<3394:mllcap>2.0.co;2.

Doyle, M.E., Barros, V.R. (2010) Attribution of the river flow growth in the Plata Basin. *International Journal of Climatology* 31, 2234–2248. doi:10.1002/joc.2228.

Ek, M.B., Mitchell, K.E., Lin, Y., Rogers, E., Grunmann, P., Koren, V., Gayno, G., Tarpley, J.D. (2003) Implementation of Noah land surface model advances in the National Centers for Environmental Prediction operational mesoscale Eta model. *Journal of Geophysical Research* 108, 8851. doi:10.1029/2002jd003296.

Garreaud, R.D., Vuille, M., Compagnucci, R., Marengo, J. (2009) Present-day South American climate. *Palaeogeography, Palaeoclimatology, Palaeoecology* 281, 180–195. doi:10.1016/j.palaeo.2007.10.032.

Georgescu, M., Lobell, D.B., Field, C.B., Mahalov, A. (2013) Simulated hydroclimatic impacts of projected Brazilian sugarcane expansion. *Geophysical Research Letters* 40, 972–977. doi:10.1002/grl.50206.

Gibbons, J.D., Chakraborti, S. (2011) Nonparametric Statistical Inference, 5th Ed. Boca Raton, FL: Chapman & Hall/CRC Press, Taylor & Francis Group.

Giles, J.A., Ruscica, R.C., Menéndez, C.G. (2020) Warm-season precipitation drivers in northeastern Argentina: Diurnal cycle of the atmospheric moisture balance and land–atmosphere coupling. *International Journal of Climatology*, 1-11 doi:10.1002/joc.6724.

Gonzalez, P.L.M., Goddard, L., Greene, A.M. (2013) Twentieth-century summer precipitation in South Eastern South America: comparison of gridded and station data. *International Journal of Climatology* 33, 2923–2928. doi:10.1002/joc.3633.

Grimm, A.M. (2003) The El Niño impact on the summer monsoon in Brazil: regional processes versus remote influences. *Journal of Climate* 16, 263-280. doi:10.1175/1520-0442(2003)016<0263:TENIOT>2.0.CO;2.

Grimm, A.M. (2004) How do La Niña events disturb the summer monsoon system in Brazil? *Climate Dynamics* 22, n.2-3, 123-138. doi:10.1007/s00382-003-0368-7.

Grimm, A.M., Pal, J., Giorgi, F. (2007) Connection between spring conditions and peak summer monsoon rainfall in South America: Role of soil moisture, surface temperature, and topography in eastern Brazil. *Journal of Climate* 20, 5929-5945. doi:10.1175/2007JCLI1684.1.

Grimm, A.M., Zilli, M.T. (2009) Interannual variability and seasonal evolution of summer monsoon rainfall in South America. *Journal of Climate* 22, 2257-2275. doi: 10.1175/2008JCLI2345.1.

Grimm, A.M. (2011) Interannual climate variability in South America: impacts on seasonal

precipitation, extreme events, and possible effects of climate change. *Stochastic Environmental Research and Risk Assessment* 25, 537–554. doi:10.1007/s00477-010-0420-1.

Grimm, A.M., Saboia, J.P.J. (2015). Interdecadal Variability of the South American Precipitation in the Monsoon Season. *Journal of Climate* 28(2), 755-775. doi:10.1175/JCLI-D-14-00046.1.

Grimm, A.M., F. Dominguez, I.F.A. Cavalcanti, T. Cavazos, M.A. Gan, P.L. Silva Dias, R.Fu, C. Castro, H.Hu, M. Barreiro. (2020) South and North American monsoons: characteristics, life cycle, variability, modelling and prediction. In: Chang, C. P., K.-J. Ha, R. H. Johnson, D. Kim, G. N. C. Lau, B. Wang (eds.), The Multi-Scale Global Monsoon System, World Scientific Series on Asia-Pacific Weather and Climate, Vol. 11, World Scientific Publishing Company, Singapore, 500 pp., Chapter 5, ISBN: 978-981-121-659-6.

Guimberteau, M., Ciais, P., Ducharne, A., Boisier, J.P., Aguiar, A.P.D., Biemans, H., Deurwaerder, H.D., Galbraith, D., Kruijt, B., Langerwisch, F., Poveda, G., Rammig, A., Rodriguez, D.A., Tejada, G., Thonicke, K., Randow, C.V., Randow, R.C.S.V., Zhang, K., Verbeeck, H. (2017) Impacts of future deforestation and climate change on the hydrology of the Amazon Basin: a multi-model analysis with a new set of land-cover change scenarios. *Hydrology and Earth System Sciences* 21, 1455–1475. doi:10.5194/hess-21-1455-2017.

Hollander, M., Wolfe, D.A. (1999) Nonparametric statistical methods. John Wiley & Sons.

Huang, B., Thorne, P.W., Banzon, V.F., Boyer, T., Chepurin, G., Lawrimore, J.H., Menne, M.J., Smith, T.M., Vose, R.S., Zhang, H.-M. (2017) Extended Reconstructed Sea Surface Temperature, Version 5 (ERSSTv5): Upgrades, Validations, and Intercomparisons. *Journal of Climate* 30, 8179–8205. doi:10.1175/jcli-d-16-0836.1.

Hurtt, G.C., Chini, L., Sahajpal, R., Frolking, S., Bodirsky, B.L., Calvin, K., Doelman, J.C., Fisk, J., Fujimori, S., Klein Goldewijk, K., Hasegawa, T., Havlik, P., Heinimann, A., Humpenöder, F., Jungclaus, J., Kaplan, J.O., Kennedy, J., Krisztin, T., Lawrence, D.,

Lawrence, P., Ma, L., Mertz, O., Pongratz, J., Popp, A., Poulter, B., Riahi, K., Shevliakova, E., Stehfest, E., Thornton, P., Tubiello, F.N., van Vuuren, D.P., and Zhang, X. (2020) Harmonization of global land use change and management for the period 850–2100 (LUH2) for CMIP6. *Geoscience Model Development*, 13, 5425–5464. doi.org/10.5194/gmd-13-5425-2020.

INPE, PRODES - Monitoramento da Floresta Amazônica Brasileira por Satélite [WWW Document]. Instituto Nac. Pesqui. Espac. website. URL. /http://www.obt.inpe.br/OBT/assuntos/programas/amazonia/prodes (accessed 9.30.2020).

Jia, G., Shevliakova, E., Artaxo, P.E., De Noblet-Ducoudré, N., et al. (2019) Chapter 2: Land–climate interactions. IPCC SRCCL 2019. pp. 131–247.

Jiménez, C., Prigent, C., Mueller, B., Seneviratne, S.I., Mccabe, M.F., Wood, E.F., Rossow, W.B., Balsamo, G., Betts, A.K., Dirmeyer, P.A., Fisher, J.B., Jung, M., Kanamitsu, M., Reichle, R.H., Reichstein, M., Rodell, M., Sheffield, J., Tu, K., Wang, K. (2011) Global intercomparison of 12 land surface heat flux estimates. *Journal of Geophysical Research* 116, D02102. doi:10.1029/2010jd014545.

Jung, M., Reichstein, M., Ciais, P., Seneviratne, S.I., Sheffield, J., Goulden, M.L., Bonan, G., Cescatti, A., Chen, J., Jeu, R.D., Dolman, A.J., Eugster, W., Gerten, D., Gianelle, D., Gobron, N., Heinke, J., Kimball, J., Law, B.E., Montagnani, L., Mu, Q., Mueller, B., Oleson, K., Papale, D., Richardson, A.D., Roupsard, O., Running, S., Tomelleri, E., Viovy, N., Weber, U., Williams, C., Wood, E., Zaehle, S., Zhang, K. (2010) Recent decline in the global land evapotranspiration trend due to limited moisture supply. *Nature* 467, 951–954. doi:10.1038/nature09396.

Kim, H., Watanabe, E.-C., Chang, K., Yoshimura, Y., Hirabayashi, J., Famiglietti, T. and Oki, T. Century long observation constrained global dynamic downscaling and hydrologic implication, n.d.

Krinner, G., Viovy, N., Noblet-Ducoudré, N.D., Ogée, J., Polcher, J., Friedlingstein, P., Ciais, P., Sitch, S., Prentice, I.C. (2005) A dynamic global vegetation model for studies of

the coupled atmosphere-biosphere system. *Global Biogeochemical Cycles* 19, GB1015. doi:10.1029/2003gb002199.

Lapola, D.M., Martinelli, L.A., Peres, C.A., Ometto, J.P.H.B., Ferreira, M.E., Nobre, C.A., Aguiar, A.P.D., Bustamante, M.M.C., Cardoso, M.F., Costa, M.H., Joly, C.A., Leite, C.C., Moutinho, P., Sampaio, G., Strassburg, B.B.N., Vieira, I.C.G. (2014) Pervasive transition of the Brazilian land-use system. *Nature Climate Change* 4, 27–35. doi:10.1038/nclimate2056.

Lawrence, D., Vandecar, K. (2015) Effects of tropical deforestation on climate and agriculture. *Nature Climate Change* 5, 27–36. doi:10.1038/nclimate2430.

Lee, S.-J., Berbery, E.H. (2012) Land-cover change Effects on the Climate of the La Plata Basin. *Journal of Hydrometeorology* 13, 84–102. doi:10.1175/jhm-d-11-021.1.

Livneh, B., Rosenberg, E.A., Lin, C., Nijssen, B., Mishra, V., Andreadis, K.M., Maurer, E.P., Lettenmaier, D.P. (2013) A Long-Term Hydrologically Based Dataset of Land Surface Fluxes and States for the Conterminous United States: Update and Extensions. *Journal of Climate* 26, 9384–9392. doi:10.1175/jcli-d-12-00508.1.

Mahmood, R., Pielke, R.A., Hubbard, K.G., Niyogi, D., Dirmeyer, P.A., Mcalpine, C., Carleton, A.M., Hale, R., Gameda, S., Beltrán-Przekurat, A., Baker, B., Mcnider, R., Legates, D.R., Shepherd, M., Du, J., Blanken, P.D., Frauenfeld, O.W., Nair, U., Fall, S. (2014) Land-cover changes and their biogeophysical effects on climate. *International Journal of Climatology* 34, 929–953. doi:10.1002/joc.3736.

Marengo, J.A., Liebmann, B., Grimm, A.M., Misra, V., Silva Dias, P.L., Cavalcanti, I.F.A., Carvalho, L.M.V, Berbery, E.H., Ambrizzi, T., Vera, C.S., Saulo, A.C., Nogues-Paegle, J., Zipser, E., Seth, A., & Alves, L. M. (2012) Recent developments on the South American monsoon system. *International Journal of Climatology*, *32*(1), 1–21. doi.org/10.1002/joc.2254.

Martens, B., Miralles, D.G., Lievens, H., Schalie, R.V.D., Jeu, R.A.M.D., Fernández-Prieto, D., Beck, H.E., Dorigo, W.A., Verhoest, N.E.C. (2017) GLEAM v3: satellite-based land evaporation and root-zone soil moisture. *Geoscientific Model Development* 10,

1903–1925. doi:10.5194/gmd-10-1903-2017.

Martens, B., Waegeman, W., Dorigo, W.A., Verhoest, N.E.C., Miralles, D.G. (2018) Terrestrial evaporation response to modes of climate variability. *npj Climate and Atmospheric Science* 1. doi:10.1038/s41612-018-0053-5.

Menéndez, C., Zaninelli, P., Carril, A., Sánchez, E. (2016) Hydrological cycle, temperature, and land surface-atmosphere interaction in the La Plata Basin during summer: response to climate change. *Climate Research* 68, 231–241. doi:10.3354/cr01373.

Menéndez, C.G., Giles, J., Ruscica, R., Zaninelli, P., Coronato, T., Falco, M., Sörensson, A., Fita, L., Carril, A., Li, L. (2019) Temperature variability and soil–atmosphere interaction in South America simulated by two regional climate models. *Climate Dynamics* 53, 2919–2930. doi:10.1007/s00382-019-04668-6.

Miralles, D.G., Berg, M.J.van den, Gash, J.H., Parinussa, R.M., Jeu, R.A.M.de, Beck, H.E., Holmes, T.R.H., Jiménez, C., Verhoest, N.E.C., Dorigo, W.A., Teuling, A.J., Dolman, A.J. (2014) El Niño–La Niña cycle and recent trends in continental evaporation. *Nature Climate Change* 4, 122–126. doi.org/10.1038/nclimate2068.

Miralles, D.G., Gentine, P., Seneviratne, S.I., Teuling, A.J. (2018) Land-atmospheric feedbacks during droughts and heatwaves: state of the science and current challenges. *Annals of the New York Academy of Sciences* 1436, 19–35. doi:10.1111/nyas.13912.

Mueller, B., Seneviratne, S.I., Jimenez, C., Corti, T., Hirschi, M., Balsamo, G., Ciais, P., Dirmeyer, P., Fisher, J.B., Guo, Z., Jung, M., Maignan, F., Mccabe, M.F., Reichle, R., Reichstein, M., Rodell, M., Sheffield, J., Teuling, A.J., Wang, K., Wood, E.F., Zhang, Y. (2011) Evaluation of global observations-based evapotranspiration datasets and IPCC AR4 simulations. *Geophysical Research Letters* 38. doi:10.1029/2010gl046230.

Müller, O.V., Berbery, E.H., Alcaraz-Segura, D., Ek, M.B. (2014) Regional Model Simulations of the 2008 Drought in Southern South America Using a Consistent Set of Land Surface Properties. *Journal of Climate* 27, 6754–6778. doi:10.1175/jcli-d-13-00463.1.

Nosetto, M., Jobbágy, E., Brizuela, A., Jackson, R. (2012) The hydrologic consequences of land-cover change in central Argentina. *Agriculture, Ecosystems & Environment* 154, 2–11. doi:10.1016/j.agee.2011.01.008.

Pereira, G., Silva, M.E.S., Moraes, E.C., Chiquetto, J.B., Cardozo, F.D.S. (2017) Improving precipitation simulation from updated surface characteristics in South America. *Theoretical and Applied Climatology* 129, 521–538. doi:10.1007/s00704-016-1800-3.

Perugini, L., Caporaso, L., Marconi, S., Cescatti, A., Quesada, B., de Noblet-Ducoudré, N., House J.I, Arneth, A. (2017) Biophysical effects on temperature and precipitation due to land-cover change. *Environmental Research Letters* 12(5), 053002. doi:10.1088/1748-9326/aa6b3f.

Pielke, R.A., Pitman, A., Niyogi, D., Mahmood, R., Mcalpine, C., Hossain, F., Goldewijk, K.K., Nair, U., Betts, R., Fall, S., Reichstein, M., Kabat, P., Noblet, N.D. (2011) Land use/land-cover changes and climate: modeling analysis and observational evidence. *Wiley Interdisciplinary Reviews: Climate Change* 2, 828–850. doi:10.1002/wcc.144.

Papastefanou, P., Zang, C.S., Pugh, T.A.M., Liu, D., Grams, T.E.E., Hickler, T., Rammig, A. (2020) A Dynamic Model for Strategies and Dynamics of Plant Water-Potential Regulation Under Drought Conditions. *Frontiers in Plant Science* 11, 1–13. doi:10.3389/fpls.2020.00373.

Prentice, I.C., Bondeau, A., Cramer, W., Harrison, S.P., Hickler, T., Lucht, W., Sitch, S., Smith, B., Sykes, M.T., n.d, (2007) Dynamic Global Vegetation Modeling: Quantifying Terrestrial Ecosystem Responses to Large-Scale Environmental Change. Terrestrial Ecosystems in a Changing World Global Change — The IGBP Series 175–192. doi:10.1007/978-3-540-32730-1_15.

Rezende, L.F.C., Arenque, B.C., Aidar, S.T., Moura, M.S.B., Randow, C.V., Tourigny, E., Menezes, R.S.C., Ometto, J.P.H.B. (2015) Evolution and challenges of dynamic global vegetation models for some aspects of plant physiology and elevated

atmospheric CO2. *International Journal of Biometeorology* 60, 945–955. doi:10.1007/s00484-015-1087-6.

Rivera, J., Penalba, O. (2014) Trends and Spatial Patterns of Drought Affected Area in Southern South America. *Climate* 2, 264–278. doi:10.3390/cli2040264.

Rodell, M., Houser, P.R., Jambor, U., Gottschalck, J., Mitchell, K., Meng, C.-J., Arsenault, K., Cosgrove, B., Radakovich, J., Bosilovich, M., Entin, J.K., Walker, J.P., Lohmann, D., Toll, D. (2004) The Global Land Data Assimilation System. *Bulletin of the American Meteorological Society*, 85(3), 381–394. doi.org/10.1175/BAMS-85-3-381.

Ruscica, R.C., Sörensson, A.A., Menéndez, C.G. (2015) Pathways between soil moisture and precipitation in southeastern South America. *Atmospheric Science Letters* 16, 267–272. doi:10.1002/asl2.552.

Ruscica, R.C., Menéndez, C.G., Sörensson, A.A. (2016) Land surface-atmosphere interaction in future South American climate using a multi-model ensemble. *Atmospheric Science Letters* 17, 141–147. doi:10.1002/asl.635.

Sakschewski, B., Bloh, W.V., Drüke, M., Sörensson, A.A., Ruscica, R., Langerwisch, F., Billing, M., Bereswill, S., Hirota, M., Oliveira, R.S., Heinke, J., Thonicke, K. (2021) Variable tree rooting strategies are key for modelling the distribution, productivity and evapotranspiration of tropical evergreen forests. *Biogeosciences* 18, 4091–4116. doi:10.5194/bg-18-4091-2021.

Salazar, A., Baldi, G., Hirota, M., Syktus, J., Mcalpine, C. (2015) Land use and land-cover change impacts on the regional climate of non-Amazonian South America: A review. *Global and Planetary Change* 128, 103–119. doi:10.1016/j.gloplacha.2015.02.009.

Saurral, R.I., Barros, V.R., Lettenmaier, D.P. (2008) Land use impact on the Uruguay River discharge. *Geophysical Research Letters* 35, L12401. doi:10.1029/2008gl033707.

Saurral, R.I., Camilloni, I.A., Barros, V.R. (2017) Low-frequency variability and trends in centennial precipitation stations in southern South America. *International Journal of Climatology* 37, 1774–1793. doi:10.1002/joc.4810.

Schaphoff, S., Bloh, W.V., Rammig, A., Thonicke, K., Biemans, H., Forkel, M., Gerten, D., Heinke, J., Jägermeyr, J., Knauer, J., Langerwisch, F., Lucht, W., Müller, C., Rolinski, S., Waha, K. (2018) LPJmL4 – a dynamic global vegetation model with managed land – Part 1: Model description. *Geoscientific Model Development* 11, 1343–1375. doi:10.5194/gmd-11-1343-2018.

Sheffield, J., Goteti, G., Wood, E.F. (2006) Development of a 50-Year High-Resolution Global Dataset of Meteorological Forcings for Land Surface Modeling. *Journal of Climate* 19, 3088–3111. doi:10.1175/jcli3790.1.

Smith, B., Wårlind, D., Arneth, A., Hickler, T., Leadley, P., Siltberg, J., Zaehle, S. (2014) Implications of incorporating N cycling and N limitations on primary production in an individual-based dynamic vegetation model. *Biogeosciences* 11, 2027–2054. doi:10.5194/bg-11-2027-2014.

Spennemann, P.C., Saulo, A.C. (2015) An estimation of the land-atmosphere coupling strength in South America using the Global Land Data Assimilation System. *International Journal of Climatology* 35, 4151–4166. doi:10.1002/joc.4274.

Spennemann, P., Salvia, M., Ruscica, R., Sörensson, A., Grings, F., Karszenbaum, H. (2018) Land-atmosphere interaction patterns in southeastern South America using satellite products and climate models. *International Journal of Applied Earth Observation and Geoinformation* 64, 96–103. doi:10.1016/j.jag.2017.08.016.

Spinoni, J., Barbosa, P., Jager, A.D., Mccormick, N., Naumann, G., Vogt, J.V., Magni, D., Masante, D., Mazzeschi, M. (2019) A new global database of meteorological drought events from 1951 to 2016. *Journal of Hydrology: Regional Studies* 22, 100593. doi:10.1016/j.ejrh.2019.100593.

Sörensson, A.A., Menéndez, C.G. (2011) Summer soil—precipitation coupling in South America. *Tellus A: Dynamic Meteorology and Oceanography* 63, 56–68. doi:10.1111/j.1600-0870.2010.00468.x.

Sörensson, A. A., Ruscica, R. C. (2018) Intercomparison and uncertainty assessment of nine evapotranspiration estimates over South America. *Water Resources Research*, 54,

2891– 2908. doi.org/10.1002/2017WR021682.

Teuling, A.J., Hirschi, M., Ohmura, A., Wild, M., Reichstein, M., Ciais, P., Buchmann, N., Ammann, C., Montagnani, L., Richardson, A.D., Wohlfahrt, G., Seneviratne, S.I. (2009) A regional perspective on trends in continental evaporation. *Geophysical Research Letters* 36, L02404. doi:10.1029/2008gl036584.

Tourigny, E. (2014) Multi-scale fire modeling in the neotropics: coupling a land surface model to a high resolution fire spread model, considering land cover heterogeneity Phd dissertation, Meteorology. INPE. http://bdtd.ibict.br/vufind/Record/INPE_9919b265a01fc91b06f0b5769b5e723e.

Tucci, C.E.M., and Clarke, R.T. (1998) Environmental issues in the La Plata Basin. *International Journal of Water Resources Development* 14(2), 157–173. doi:10.1080/07900629849376.

Vera, C., Higgins, W., Amador, J., Ambrizzi, T., Garreaud, R., Gochis, D., Gutzler, D., Lettenmaier, D., Marengo, J., Mechoso, C.R., Nogues-Paegle, J., Dias, P.L.S., Zhang, C. (2006) Toward a Unified View of the American Monsoon Systems. *Journal of Climate* 19, 4977–5000. doi:10.1175/jcli3896.1.

Vera, C.S., Díaz, L. (2015) Anthropogenic influence on summer precipitation trends over South America in CMIP5 models. *International Journal of Climatology* 35, 3172–3177. doi:10.1002/joc.4153.

Wang, K., Dickinson, R.E. (2012) A review of global terrestrial evapotranspiration: Observation, modeling, climatology, and climatic variability. *Reviews of Geophysics* 50, RG2005. doi:10.1029/2011rg000373.

Weedon, G.P., Gomes, S., Viterbo, P., Shuttleworth, W.J., Blyth, E., Österle, H., Adam, J.C., Bellouin, N., Boucher, O., Best, M. (2011) Creation of the WATCH Forcing Data and Its Use to Assess Global and Regional Reference Crop Evaporation over Land during the Twentieth Century. *Journal of Hydrometeorology* 12, 823–848. doi:10.1175/2011jhm1369.1.

Weedon, G.P., Balsamo, G., Bellouin, N., Gomes, S., Best, M.J., Viterbo, P. (2014) The

WFDEI meteorological forcing data set: WATCH Forcing Data methodology applied to ERA-Interim reanalysis data. *Water Resources Research* 50, 7505–7514. doi:10.1002/2014wr015638.

Zhang, H., Delworth, T.L., Zeng, F., Vecchi, G., Paffendorf, K., Jia, L. (2016a) Detection, Attribution, and Projection of Regional Rainfall Changes on (Multi-) Decadal Time Scales: A Focus on Southeastern South America. *Journal of Climate* 29, 8515–8534. doi:10.1175/jcli-d-16-0287.1.

Zhang, Y., Peña-Arancibia, J.L., McVicar, T.R., Chiew, F.H.S., Vaze, J., Zheng, H., Wang, Y. (2016b) Monthly global observation-driven Penman-Monteith-Leuning (PML) evapotranspiration and components. v2. CSIRO. Data Collection. doi:10.4225/08/5719A5C48DB85.

Zhang, Y., Peña-Arancibia, J.L., Mcvicar, T.R., Chiew, F.H.S., Vaze, J., Liu, C., Lu, X., Zheng, H., Wang, Y., Liu, Y.Y., Miralles, D.G., Pan, M. (2016c) Multi-decadal trends in global terrestrial evapotranspiration and its components. *Scientific Reports* 6, 19124. doi:10.1038/srep19124.

Abbreviation	Complete name and key characteristics of datasets	References
Dynamic Global Vegetation Models (DGVMs)		
INLAND	INtegrated model of LAND surface processes (INPE, São José dos Campos, Brazil) *Timestep*: 30min. *Atmos. forcing variables*: Tmax, Tmin, P, swdwn, lwdwn, w, q. *Maximum soil depth*: 4 m. *#PFTs*: 16	Tourigny et al. (2014)
LPJmL4	Lund Potsdam Jena managed Land model (version 4.0) (PIK, Potsdam, Germany) *Timestep*: daily. *Atmos. forcing variables*: T, P, swdwn, lwnet. *Maximum soil depth*: 3 m. *#PFTs*: 11	Schaphoff et al. (2018)
LPJ-GUESS	Lund-Potsdam-Jena General Ecosystem Simulator (version 4.0.1) (Lund University, Lund, Sweden) *Timestep*: daily. *Atmos. forcing variables*: T, P and swdwn. *Maximum soil depth*: 1.5 m. *#PFTs*: 13 (5 in the tropics)	Smith et al. (2014)
ORCHIDEE	ORganising Carbon and Hydrology In Dynamic EcosystEms (version 2.0) (IPSL, Paris, France) *Timestep*: 30min. *Atmos. forcing variables*: T, P, swdwn, lwdwn, w, q. *Maximum soil depth*: 2m. *#PFTs*: 13	Krinner et al. (2005)
Atmospheric forcing datasets (0.5°x0.5°)		
GLDAS_2.0	Global Land Data Assimilation System (v2). http://ldas.gsfc.nasa.gov/gldas	Rodell et al. (2004)
GSWP3	Global Soil Wetness Project Phase 3. http://hydro.iis.u-tokyo.ac.jp/GSWP3/exp1.html	Kim et al. n. d.
WATCH+WFDEI	The WFDEI Meteorological Forcing Data as used in the ISIMIP project https://www.isimip.org/gettingstarted/input-data-bias-correction/details/5/	Weedon et al. (2011, 2014)
Evapotranspiration reference datasets		
GLDAS_2.0	Global Land Data Assimilation System (v2) with Noah Land Surface Model. http://ldas.gsfc.nasa.gov/gldas. Available between 1948 and 2010	Ek et al. (2003), Rodell et al. (2004), Sheffield et al. (2006)
GLEAM_3.3a	Global Land Evaporation Amsterdam Model. Version 3a. https://www.gleam.eu. Available between 1980 and 2010	Martens et al. (2017)
PML	Observation-driven Penman–Monteith–Leuning model. https://data.csiro.au/dap/. Available between 1980 and 2010	Zhang et al. (2016b)
Land-cover change data (1km^2)		
LCC	PRODES (INPE-PRODES 2019) in Brazilian Amazon and Cerrado, IBGE rest of Brazil, and LUH2 (Land use Harmonization) in the rest of the South American countries.	INPE, PRODES. Hurtt et al. (2020)

Table 1: Summary of key characteristics of DGVMs, atmospheric forcing variables, and land-cover change datasets used for simulations; and evapotranspiration reference datasets. T refers to surface air temperature, Tmax and Tmin refer to surface air maximum and minimum temperatures respectively, P to precipitation, swdwn to shortwave downward radiation, lwdwn to long wave downward radiation, lwnet to long wave net radiation, w to wind speed and q to air specific humidity. #PFTs indicates the number of plant functional types.

	+EOF1	-EOF1	-	Total
EN	1966, 1973/7, 1998, 2010	1952, 1964	1954/8/9, 1969, 1970/8, 1980/3/7/8, 1992/5, 2003/5/7	**22**
LN	1971/4, 1984, 2001	1965, 1985, 2009	1955/6, 1972/5/6, 1989, 1996/9, 2000/6/8	**18**
Neutral	1981	1957, 1960/2/8, 1979	rest of 14 DJFs	
Total	**10**	**10**		

Table 2: Austral summers (DJFs) identified as EOF1s (columns) and/or ENSO (rows) events during the analyzed 1951–2010 period. EOF1 events are based on precipitation forcings, while ENSO events are taken from the NOAA´s CPC website (see section 2.3. for details). The year label corresponds to that of February, for example, 1956 refers to the summer of 1955–1956.

Romina C. Ruscica, Fig.1, top of the figure

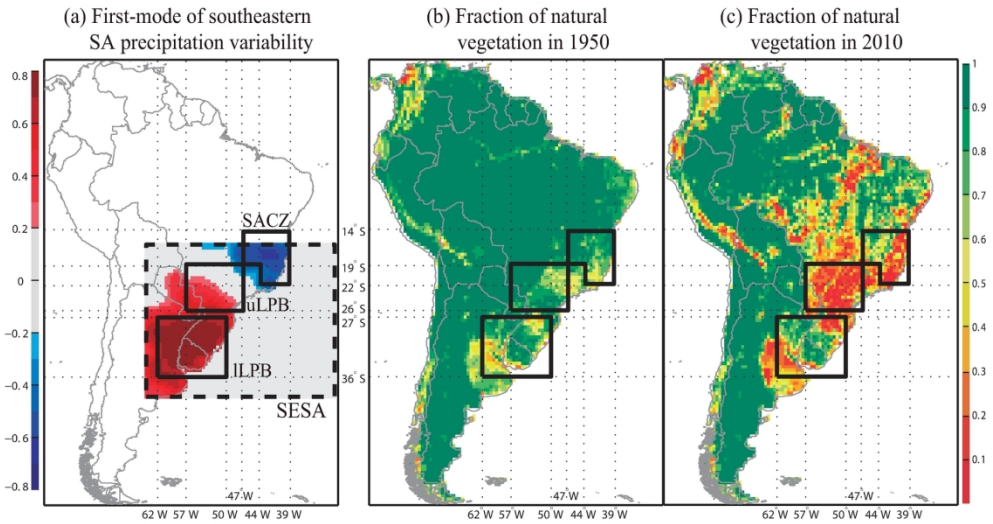

Fig. 1: (a) Correlation pattern (p-value<0.05) between DJF precipitation and the temporal evolution of the subtropical EOF1 calculated for southeastern South America (SESA, dashed rectangle) using GLDAS_2.0 dataset (see section 2.3 for details). Black lines indicate the three regions under study: South Atlantic Convergence Zone (SACZ), upper La Plata Basin (uLPB), and lower La Plata Basin (lLPB). Fraction of natural vegetation in (b) 1950 and (c) 2010, representing the land-cover change undergone by the continent.

Romina C. Ruscica, Fig.2, top of the figure

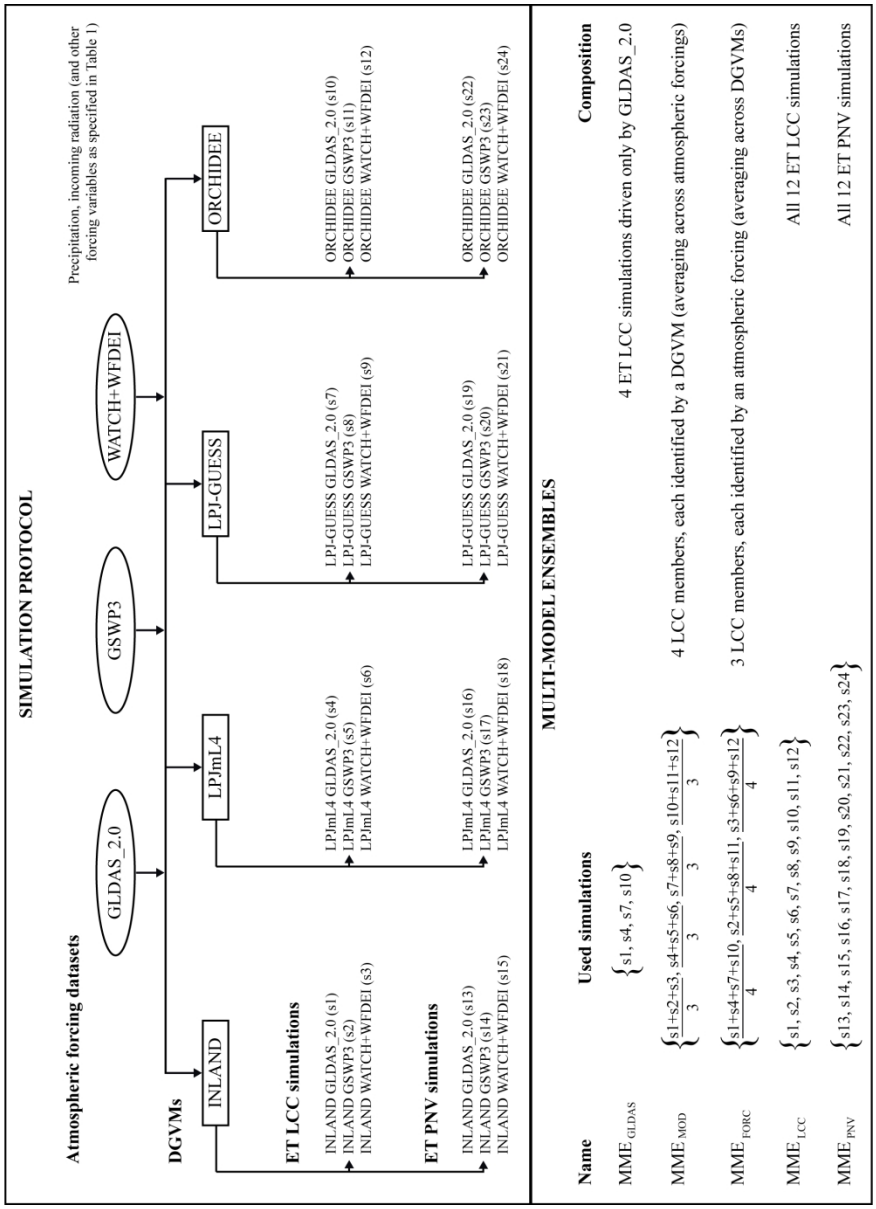

Fig. 2. (Top) Diagram of simulation protocol: Evapotranspiration (ET) simulations obtained from four DGVMs forced by three atmospheric datasets, under two conditions: observed land-cover changes (LCC) and potential natural vegetation (PNV). The 24 ET simulations (s) are tagged with a number, e.g., the ET simulation from LPJmL4 DGVM forced by GSWP3 under the LCC scenario is defined as 's5.' (Bottom) Multi-model ensemble definitions: Five multi-model ensembles (MME) are combinations of 24 simulations. MMEs use only land-cover change simulations, except MME_{PNV}.

Romina C. Ruscica, Fig.3, top of the figure

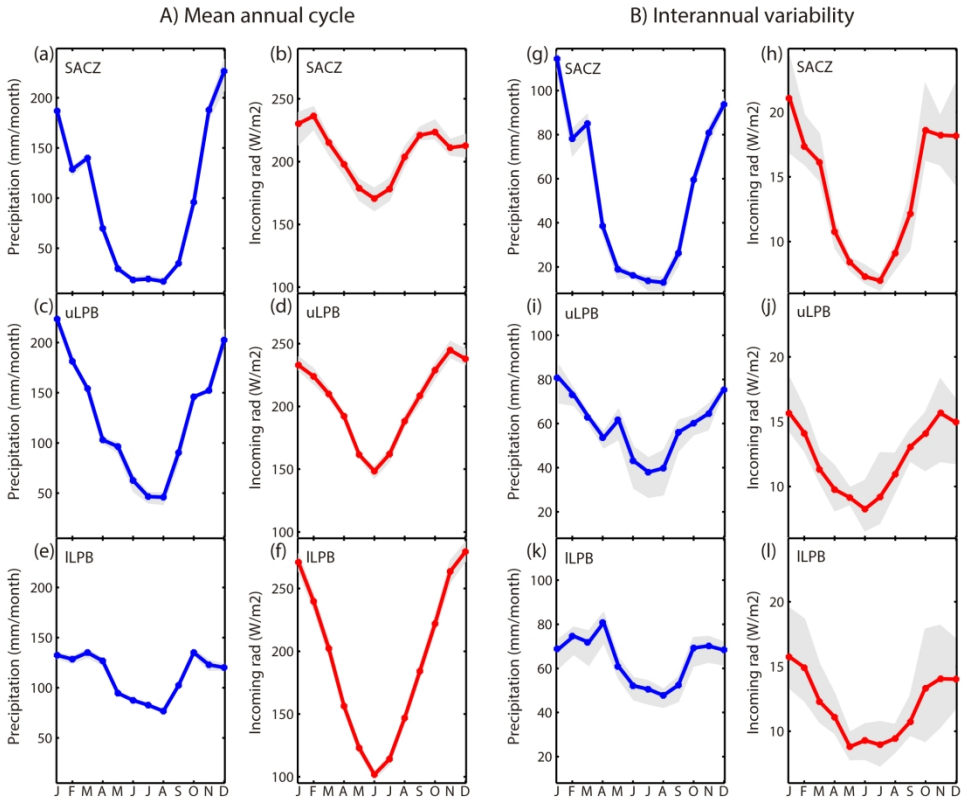

Fig. 3. Annual cycles of precipitation (blue) and incoming radiation (red) of the three atmospheric forcings (Table 1) for each region under study (rows), in 1950–2010. Spread (measured as maximum–minimum) in grey and mean in full lines. Monthly means are shown in A) and monthly standard deviations as an indicator of interannual variability in B).

Romina C. Ruscica, Fig.4, top of the figure

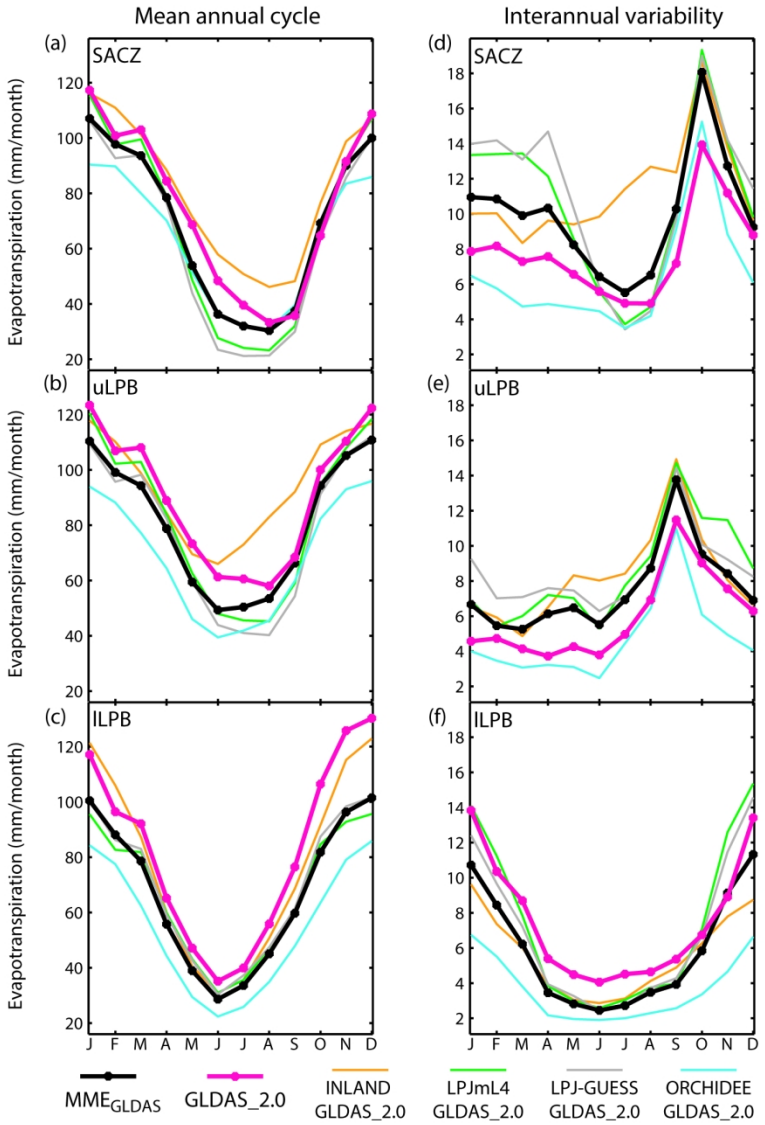

Fig. 4. Annual cycles of evapotranspiration (mm/month) of the MME_{GLDAS} members (mean in black line) and GLDAS_2.0 (magenta line) for each region (rows), in 1950–2010. Left: monthly means. Right: monthly standard deviations as an indicator of interannual variability.

Romina C. Ruscica, Fig.5, top of the figure

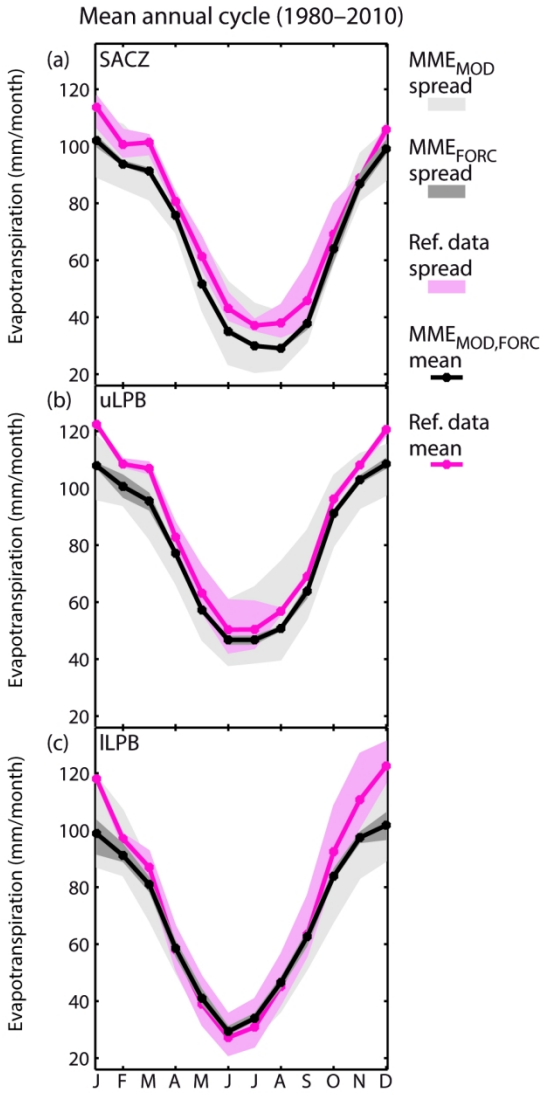

Fig. 5. Mean evapotranspiration (ET) annual cycles from MME_{MOD} and MME_{MOD} (spread in grey and means in black lines) compared to ET reference datasets (spread in light magenta and means in magenta lines), for each region (rows), in 1980–2010 (mm/month). Note that means (black lines) of MME_{MOD} and MME_{FORC} are equal and the same as MME_{LCC} (see section 4.2 for details).

Romina C. Ruscica, Fig.6, top of the figure

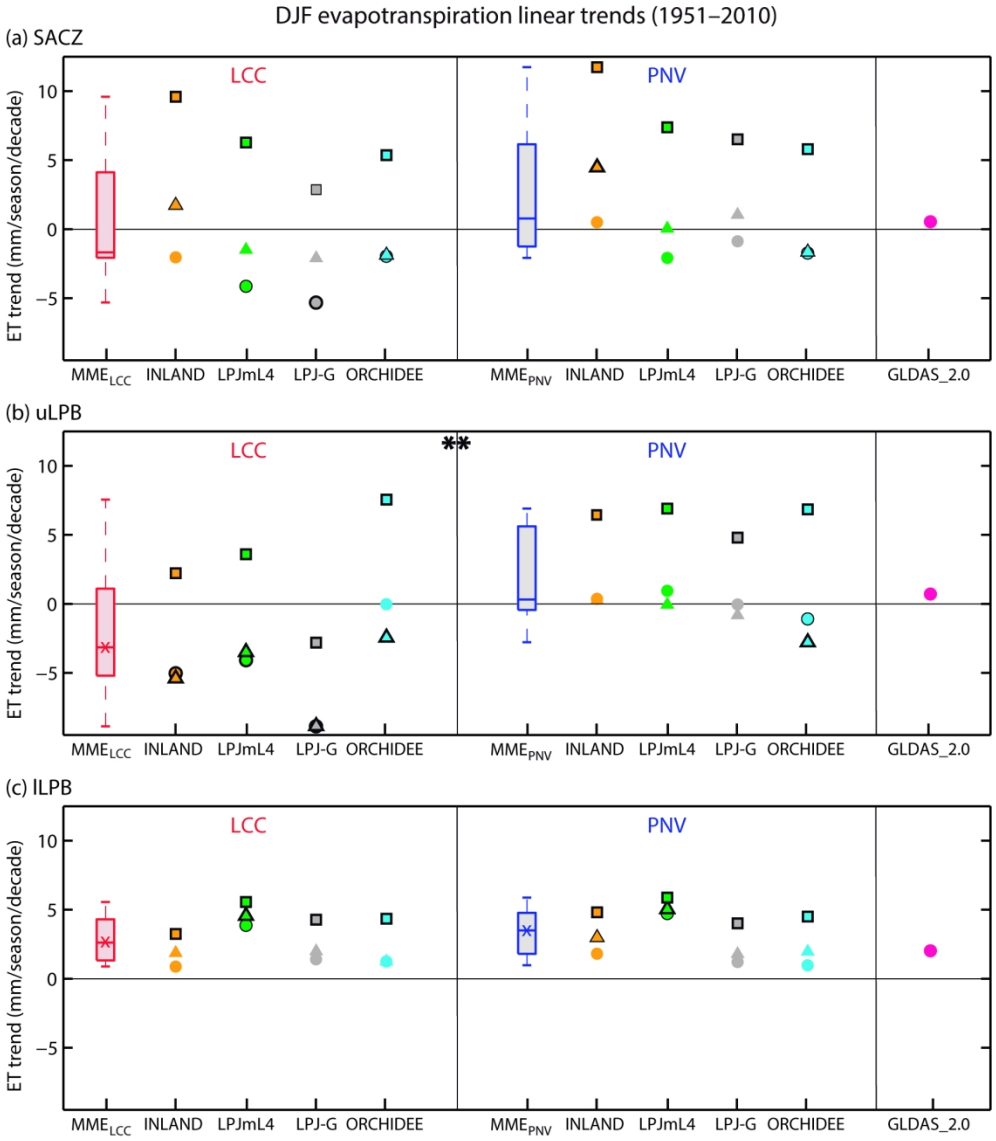

Fig. 6. Summer (DJF) ET linear trend slopes of both MME (boxplots, LCC in red and PNV in blue) for each region (rows), in 1951–2010. The bottom, middle and top of each boxplot are the 25th, 50th, and 75th percentiles, respectively. Bottom and top whiskers represent minimum and maximum values. Wilcoxon rank test detects MME medians that are different from 0 (x), and between LCC and PNV scenarios (**) ($p<0.15$). Individual ET trends for each DGVM driven by the GLDAS_2.0 (circles), GSWP3 (triangles) or WATCH+WFDEI (squares) atmospheric forcings, and GLDAS_2.0 ET reference dataset (magenta circle). Significant trends have black borders (thinner for $p<0.2$ and thicker for $p<0.05$).

Romina C. Ruscica, Fig.7, top of the figure

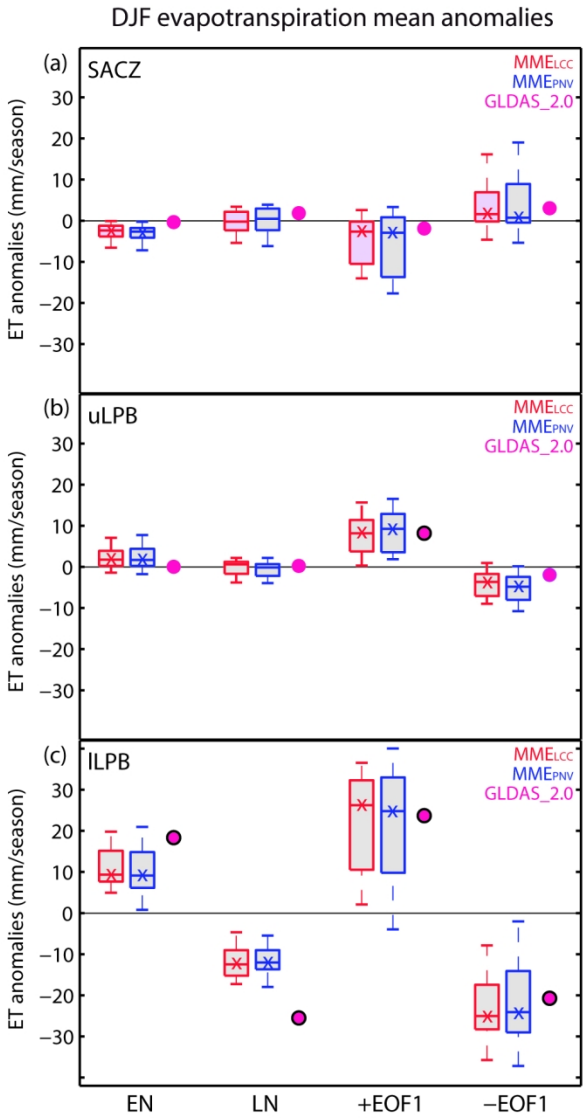

Fig. 7: Composite of linear detrended summer ET mean anomalies of both MME (LCC in red and PNV in blue) under El Niño (EN), La Niña (LN), positive and negative EOF1 DJF, for each region (rows), in 1951–2010. Wilcoxon rank test detects MME medians that are different from 0 (x), and between LCC and PNV scenarios (**, none in this case) ($p<0.15$). Magenta dots: similar GLDAS_2.0 anomalies. Black borders: means different from 0 in GLDAS_2.0 ($p<0.08$).

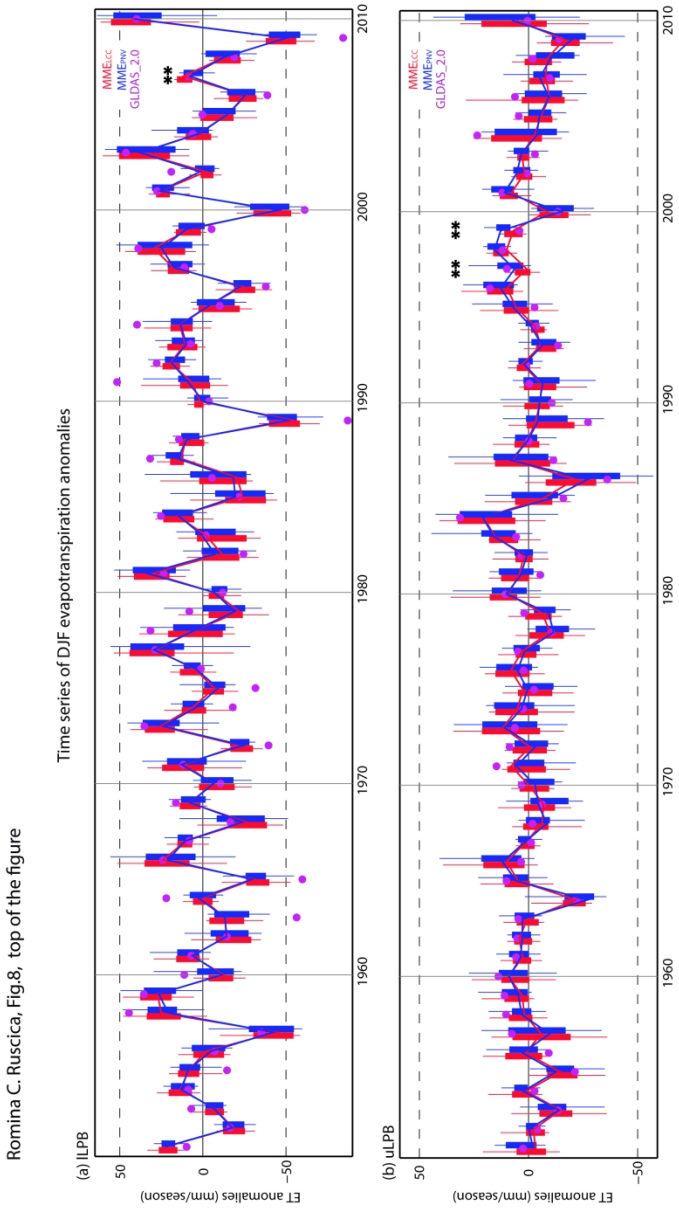

Fig. 8: Linear detrended summer ET anomalies of both MME (LCC in red and PNV in blue) in (a) lLPB and (b) uLPB regions. Full lines: temporal evolutions of MME medians. Outliers were removed for clear visualization of results. Wilcoxon rank test detects MME medians that are different between LCC and PNV scenarios (**, $p<0.15$). Magenta dots: similar GLDAS_2.0 anomalies. The year label corresponds to February (e.g., 1960 refers to the DJF of 1959–1960). Notice that vertical ranges are different.

Romina C. Ruscica, Fig.9, top of the figure

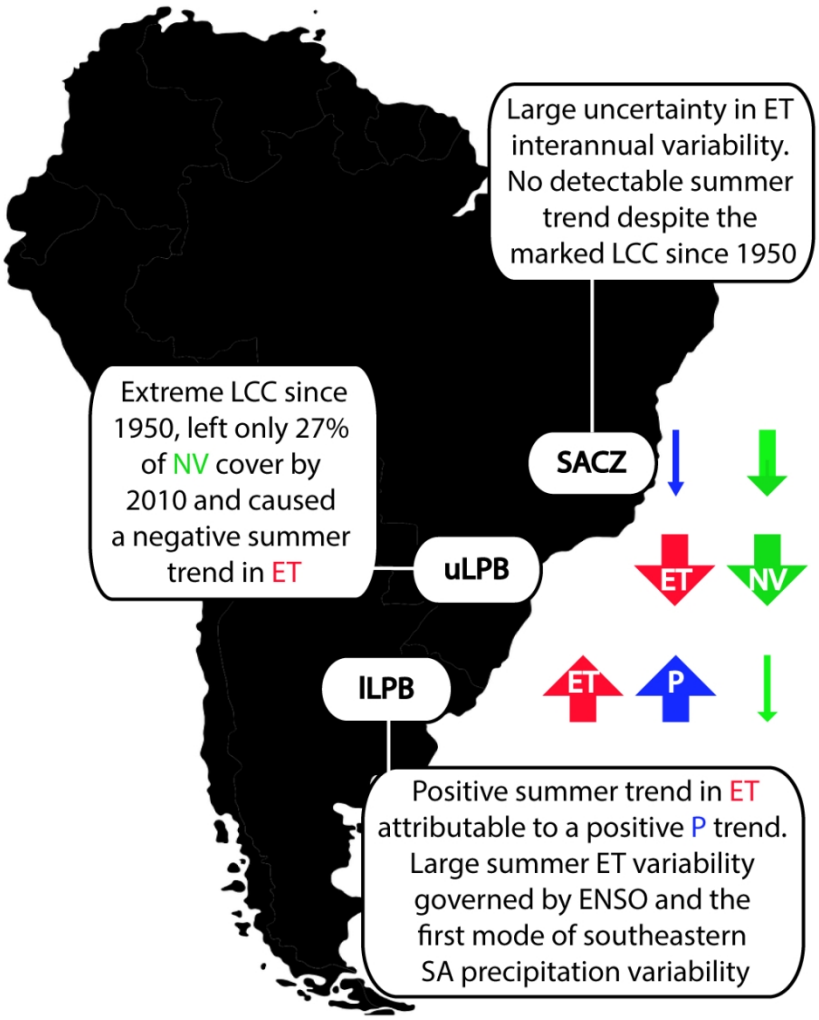

Fig. 9: Summary of main findings in each region. Arrows indicate trends in evapotranspiration (ET), precipitation (P), and fraction of natural vegetation (NV). Arrows with letters indicate trends that are statistically significant. LCC: land-cover change.